Impact of convection and radiation on direct/hybrid heating stability of field assisted sintering

Charles Manière, Flora Borie, Sylvain Marinel

Impact of convection and radiation on direct/hybrid heating stability of field assisted sintering

Charles Manière[a]*, Flora Borie[a], Sylvain Marinel[a]

(a) Normandie Univ, ENSICAEN, UNICAEN, CNRS, CRISMAT, 14000, Caen, France

Keywords
Thermal Instability; Multiphysics Modeling; Hybrid Heating; Sintering; Ceramic

Abstract

Field assisted sintering (FAST) processes allow a direct transmission of the heating energy to the specimen (through the electric, magnetic fields or the electrical current). FAST allows higher heating rates, faster sintering response and a better control of the sintered microstructures. However, FAST suffers high heating instability in direct heating configurations which generally takes the form of a hot spot. The origin of these hot spots is well known and is correlated to the convective/radiative cooling at the specimen surfaces and the thermal dissipation in the specimen. Nevertheless, the impact of these cooling fluxes evolves with the sample dimensions, thermal insulation, heating rate and hybrid heating conditions and there is not clear quantification of the relative importance of these fluxes in regards to the previous cited heating conditions. In this work we develop a finite element (FE) tool which can easily explore the heating stability of an "Equivalent Thermal Cavity" (ETC). We illustrate the ETC concept by the case study of the microwave sintering of zirconia. We show that the dominant heat transfer is radiative, but the convective fluxes have a high importance for the temperatures homogenization, in particular in the case of a hybrid heating configuration.

* Corresponding author: **CM**: Laboratoire de cristallographie et sciences des matériaux (CRISMAT), 6 Bvd du maréchal Juin 14050 CAEN CEDEX 4, France
Ph.: +33.2.31.45.13.69 ; *E-mail address*: charles.maniere@ensicaen.fr

Nomenclature

ρ Density (kg/m^3)
C_p Heat capacity (J/(kg.K))
T Temperature (K)
κ Thermal conductivity (W/(m.K))
Q Heat source (W/m^3)
𝕚 identity tensor
$\boldsymbol{u}$ Velocity vector (m/s)
μ Dynamic viscosity (Pa.s)
$\boldsymbol{F_g}$ Body force term (N/m^3)
Q_p Pressure heat source term (W/m^3)
Q_{vd} Viscous dissipation heat source term (W/m^3)
φ_{rsa} Surface to ambient radiative heat flux (W/m^2)
σ_s Stefan Boltzmann constant (5.67E-8 W.m^{-2}K^{-4})
ϵ Emissivity
T_{air} Air temperature (K)
φ_{csa} Convective heat flux (W/m^2)
h_{ia} Surface conductivity (W/(m^{2}K))
J Surface radiosity (W/m^2)
G Irradiation flux (W/m^2)
n Refractive index
$e_b(T)$ Surface radiation produced (W/m^2)
ρ_r Reflectivity
φ_{rss} Net inward radiative heat flux (W/m^2)
Q_{PID} PID regulated heat source (W/m^3)
$e(t)$ Regulated -measured temperature error (K)
K_p PID proportional coefficient
K_I PID integral coefficient
K_D PID derivative coefficient

1. Introduction

Field assisted sintering (FAST) approaches such as microwave sintering, inductive sintering, or spark plasma sintering obey a complex Multiphysics problem including[1–4]: electromagnetic fields, electrical current, heat transfer and sintering. The complex coupling between all these Multiphysics parameters is a cause of instabilities like field concentration, thermal runaway, thermal gradients[5–9]. However, the most detrimental phenomenon is the formation of hot spots[10–12]. Materials having a dissipative parameter which increases with temperature (like for negative temperature coefficient resistivity NTC materials) tends to experience hot spots in direct heating[13]. This is due to the surfaces cooling implying higher

center specimen temperature. In addition, for NTC materials like zirconia, the higher the temperature rises, the greater is the heat dissipation[14]. Consequently, the thermal instabilities originated from the surfaces cooling are amplified by the NTC behavior of some materials, ending with hot spot formation and thermal runaway[15]. This problem is particularly present in flash sintering. In addition to previous cited thermal inhomogeneity problems, this new field assisted and ultra-rapid sintering approach experiments abrupt sintering and thermal profiles which end up with inherent instabilities[7,16–19]. In flash sintering, the homogeneity problem is a key issue necessary for the scalability of this phenomenon[20]. In order to stabilize FAST processes, hybrid heating approaches are generally investigated. In microwave sintering, a susceptor (a material which strongly couples with microwaves) is generally employed to initiate the specimens heating and homogenize the temperature field by reducing the specimen natural cooling from its surface[21,22]. Simulation works have been done to evaluate the direct/hybrid heating and the homogeneity of the temperature field, but these studies are generally limited to the heating and does not take into account the air convection[4,15,23–27].

All these FAST processes need to be stabilized through a better understanding of their cooling mechanisms and the help of a predictive simulation tool. The finite element simulation is generally employed to detect the dominant heat transfer parameter and predict optimization configurations. However, the high Multiphysics nature of FAST process makes this task difficult. For instance, a comprehensive microwave sintering model requires implementing an electromagnetic part, for the microwave distribution in the cavity, thermal/fluid dynamic parts for the heat transfer by conduction/radiation/convection[28] and a mechanical part, for the sintering and a numerical PID to regulate the system[15]. All these physics have parameters coupled to each other and represent a challenge of computation stability and time.

In this context, we develop a modeling approach called “ETC”, standing for “Equivalent Thermal Cavity”, consisting of a cavity where it is simple to investigate the impact of the

cooling fluxes and different parameters (dimensions, heating rates, susceptors) on the heating homogeneity. This work focuses on the hot spot formation during the direct/hybrid heating of a regular shape specimen and the study of the contribution of the radiative/convective cooling fluxes. In the following, we will describe first the finite element ETC model and how the different heat fluxes are calculated. Then, the results of the ETC model for the different parameters will be presented and discussed.

2. Theory and calculations

The ETC model governing equations is presented first, and is followed by the description of the main boundary conditions.

2.1. Heat transfer in the solid and gas

Heat transfer is different whether if considered in fluid or solid. In solid parts, no convection phenomenon is possible, then heat is classically described by [5]:

$$\rho C_p \frac{\partial T}{\partial t} + \nabla.(-\kappa \nabla \mathrm{T}) = Q \qquad (1).$$

In the fluid part like the gas area in a furnace, two additional heat transfers should be taken into account, the surface to surface thermal radiation which is here considered by boundary conditions (see next section) and the natural convection of the air which requires additional fluid dynamic equations. The convection is a key point for heat transfer problems like a furnace and heating system because the convective fluxes can be a source of intense cooling[29] or of homogenization when heating elements (or susceptors) are used[28]. The Navier-Stokes convective problem is employed and is defined by the following three main governing equations[30]:

the mass conservation equation:

$$\frac{\partial \rho}{\partial t} + \nabla.(\rho \boldsymbol{u}) = 0 \quad (2)$$

the momentum equation where appears the pressure, viscous and body forces terms:

$$\rho\left(\frac{\partial \mathbf{u}}{\partial t} + \boldsymbol{u}.\nabla \boldsymbol{u}\right) = -\nabla p + \nabla.\left(\mu(\nabla \mathbf{u} + (\nabla \mathbf{u})^T) - \frac{2}{3}\mu(\nabla.\mathbf{u})\mathbb{i}\right) + \boldsymbol{F_g} \quad (3)$$

and the energy balance equation which is the equivalent of the heat equation in fluid and takes into account the convective term and the additional pressure Q_p and viscous dissipation Q_{vd} heat source term which are often very low and neglected for our application:

$$\rho C_p\left(\frac{\partial T}{\partial t} + (\boldsymbol{u}.\nabla)T\right) + \nabla.(-\kappa \nabla T) = Q + Q_p + Q_{vd} \quad (4).$$

2.2. Boundary conditions

A scheme of the "Equivalent Thermal Cavity" (ETC) is reported in figure 1a. The ETC model is an insulation box cavity where a cylindrical zirconia specimen and eventual susceptor are placed. We consider the 2D axisymmetric approximation to reduce the computation time.

The external insulation box boundaries are subjected to convective and surface to ambient cooling fluxes described by the equations:

$$\varphi_{rsa} = \sigma_s \epsilon({T_{air}}^4 - T^4) \quad (5)$$

$$\varphi_{csa} = h_{ia}(T_{air} - T) \quad (6).$$

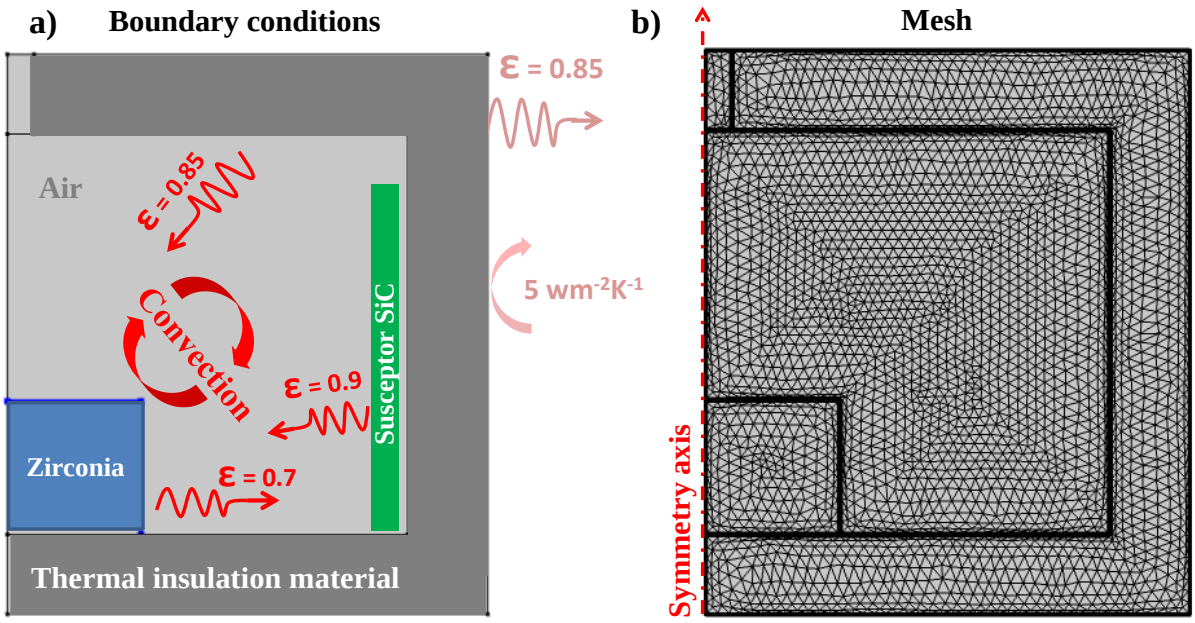

Figure 1 a) Scheme of the equivalent thermal cavity with the values of the boundary parameters, b) mesh.

The inner solid/air interfaces are subjected to the fluid dynamics part where "wall" no penetration conditions are used and to the mutual surface-to-surface radiation which considers each material emissivity. The surface to surface radiation can be defined by the total outgoing radiative flux (called radiosity) *J* which includes the irradiated power $e_b(T)$ and the incoming irradiation G:

$$J = \rho_r G + \epsilon e_b(T) = \rho_r G + \epsilon n^2 \sigma_s T^4 \quad (7)$$

by the ideal gray body simplification, we have:

$$\epsilon = 1 - \rho_r \quad (8)$$

the expression of the net inward radiative heat flux φ_{rss} is:

$$\varphi_{rss} = \epsilon(G - e_b(T)) \quad (9).$$

For this study, we use a triangular mesh with refinement at the interfaces (figure 1b). Classically, the temperature is measured by a pyrometer on the top of the specimen through the upper hole of the insulation box. In the model, the temperature upper specimen temperature is regulated through a proportional integral derivative (PID) numerical regulator

which changes the value of the specimen heat source term Q_{PID} to follow a constant heating rate of 10 K/min. The PID expression is as follows.

$$Q_{PID} = K_p e(t) + K_I \int_0^t e(t)d\tau + K_D \frac{de(t)}{dt} \quad (20)$$

3. Experiment and method

The "Equivalent Thermal Cavity" (ETC) is used to simulate the impact of the main heat transfer mechanism in the formation of hot spot and heating instabilities for the FAST sintering approaches. In our method, we do not model the fields or current distribution in the material which are assimilated to a uniform dissipation term which is PID regulated (the term Q_{PID}). Instead, we focus on the different radiative/convective heat fluxes in the cavity that we suspect to be mainly responsible for the hot spot formation and the heating heterogeneity. The ETC configuration (figure 1a) has the potential to approximate the heating homogeneity of most of the FAST approach by adjusting the cavity dimensions to the equivalent specimen, insulation, heating element and air volumes. In this work, we will test the microwave heating response of a 50 % dense zirconia specimen placed in an insulation box cavity. The reference thermal cycle of the simulation work is a 10 K/min heating ramp from room temperature to 1000 °C. Indeed, the heating rate value of 10 K/min is considered as fast for conventional sintering and lower range for field assisted sintering. For simplicity, the simulation study does not consider sintering starting at 1000 °C, the thermal simulations are then stopped at this temperature. For direct microwave heating, the microwave thermal dissipation in the zirconia sample is modeled by Q_{PID}. For hybrid heating, a silicon carbide (SiC) susceptor is generally added next to the specimen. The susceptor couples more with microwaves than the zirconia sample; in our case it will be modeled by a dissipation term $Q_{PID}.Fc$, where Fc is a multiplicative factor which increase or reduce the dissipation in the susceptor. With the help of the ETC model, we will test the impact of the sample dimension, heating rate and hybrid

heating on the heating stability of the zirconia specimen. The temperature dependence properties of zirconia, silicon carbide and the insulation material can be found in our previous work in ref[15,27].

We report in figure 2 an initial case of 10 K/min direct heating where it can be seen the temperature distribution (figure 1a) and the convective velocity field (figure 1b). In order to estimate the relative magnitude of the cooling fluxes of the zirconia sample, we calculate the integral of the radiative and convective fluxes in the solid/air interfaces and the integral of the zirconia/insulation interface conductive flux (see figure 1c). This gives the curves reported in figure 1d in watts. Using these curves, it is possible to determine the ratio of each of these three fluxes contribution *versus* temperature, giving the graph reported in figure 1e.

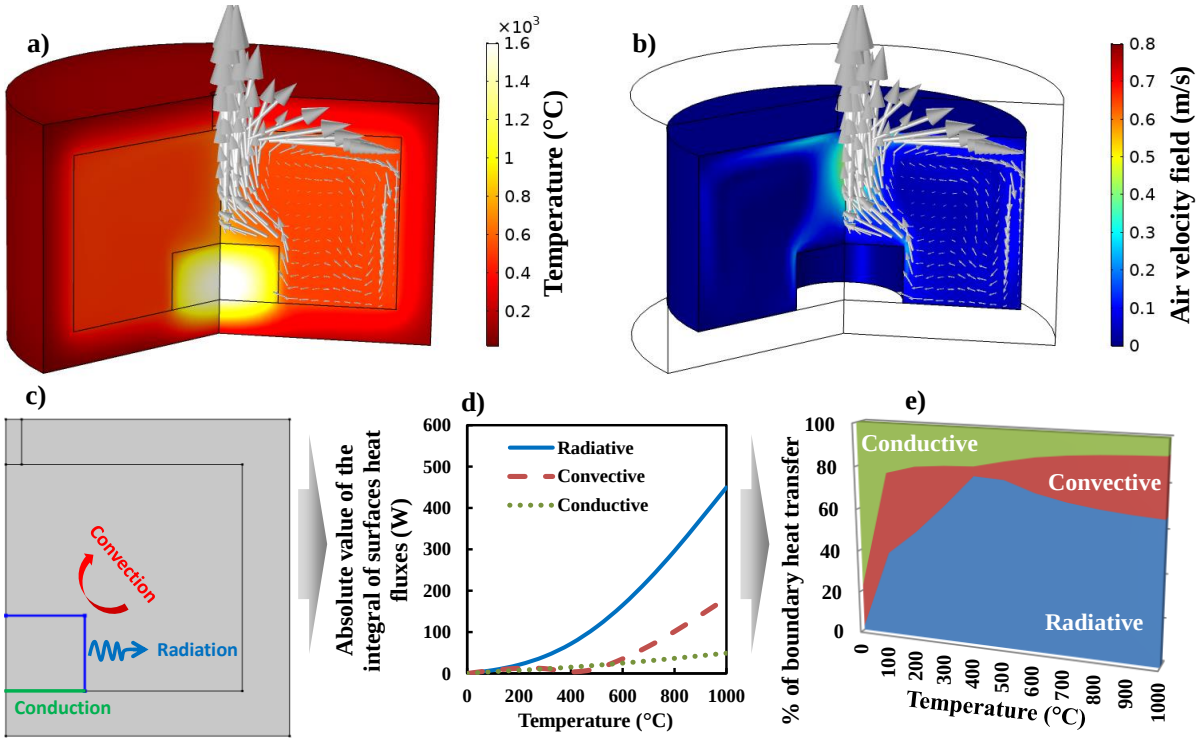

Figure 2 Direct 10 K/min heating of a zirconia specimen; a) temperature and b) convection velocity field at the end of the cycle; c) scheme of the specimen interfaces considered in the specimen cooling fluxes analysis, d) integral of the specimen cooling fluxes through the specimen surfaces, e) cooling fluxes ratio diagram.

In order to illustrate our simulation results, we conduct three microwaves sintering experiments in different heating conditions. Two direct heating configurations will test the

heating with radiation/convection cooling fluxes and in thermal insulation condition. The third experiment will undergo the hybrid sintering mode using silicon carbide susceptors. The microwave experiments use SAIREM 2.45 GHz TE10 single-mode configuration. We employed Tosoh TZ-3YB-E zirconia powder (3 mol% Y_2O_3, specific surface area 16 ± 3 m^2/g, particle size 40 nm[31]) to obtain 50% dense 12 mm green pellets after die pressing (with a hydraulic press "Specac GS1501", under an applied pressure of 1 ton).

4. Results and discussions

In this section is presented, the outcome of the ETC simulation in different direct and hybrid heating configurations.

4.1. Direct heating cooling fluxes

The initial direct heating model presented in figure 2 leads to the formation of a hot spot into the zirconia sample. This result is consistent with temperature differences (Tmax-Tmin) as high as ~ 1000 K (figure 2a). It is clear from figures 2a and figures 2e that the solid/air interface represents the highest cooling fluxes with a contribution of about 60% of radiation and 30% of convection. The conductive flux from the sample to the support is low, explaining why the hot spot is near this interface. The cooling convection fluxes homogenize the heat in the cavity through gas convection velocities between 0.1-0.3 m/s. The convection fluxes follow a circular motion where a fraction of the heat loss from the sample is coming back. This phenomenon partially stabilizes the heating and explains why the convection contribution is only 30%. This mechanism also explains why convective cooling fluxes can be high when the specimen is placed in a large cavity[29]. To check the impact of the surface to surface radiation on the hot spot formation, we simulate the direct heating case, reported in figure 1, without the convection in the gas. The ETC cavity is assumed to be in vacuum with

pure radiation in the inner surfaces, the results are reported in figure 3. The temperature field shows that the thermal radiation from the specimen raises the temperature of the adjacent insulation box inner surfaces. The proportion of the specimen radiative cooling flux is 90% at the end of the cycle. A hot spot is still observed in the specimen at the end of the cycle, with a temperature difference Tmax-Tmin = 1008 K which is closed to the previous case with convection.

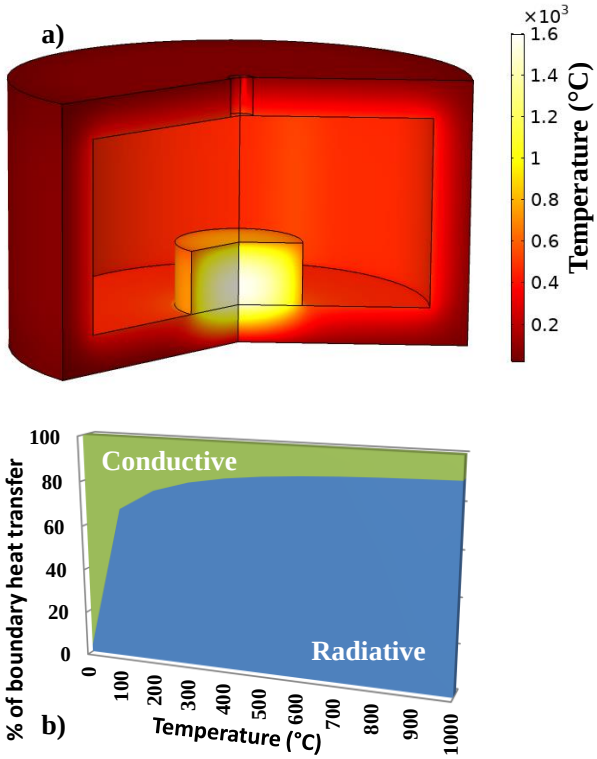

Figure 3 Direct 10 k/min heating configuration in vacuum (without convection), a) simulated temperature field at the end of the cycle and b) the simulated specimen cooling fluxes diagram.

In direct heating, the thermal inhomogeneity is high and originates from an important cooling at the sample surfaces by radiation and/or convection. In the following, we will try two approaches to stabilize the direct heating inhomogeneity. One by reducing the air volume in the cavity (reduction of convective cooling flux) and another by delaying the hot spot formation using high heating rates.

4.2. Impact of dimension and cavity filling in the heating stabilization

Increasing the dimensions of the specimen in the reference configuration figure 2a decreases the air volume in the cavity. We expect that this parameter reduces the cooling fluxes by convection and also by radiation as the insulator surface becomes very close to the specimen. The ETC results are reported in figure 4 where the cavity filling ratio is increased from the reference configuration (11%) to 87%. In figure 5 are reported, the specimen temperature curves corresponding to the reference configuration (such as in figure 2) and the graph of the specimen temperature difference and average cavity material temperatures.

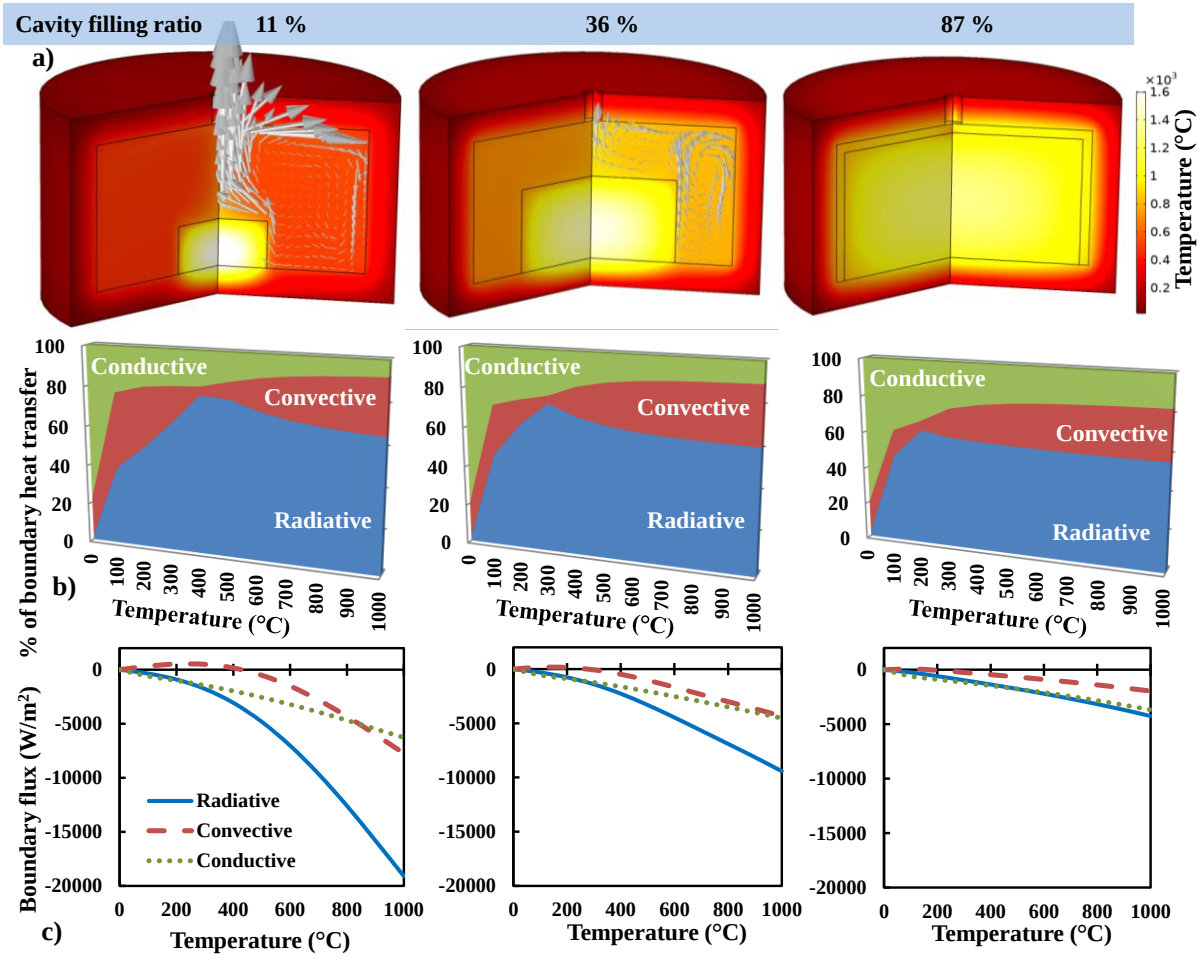

Figure 4 Simulation of the ETC configuration for different cavity filling ratio, a) simulated temperatures at the end of the cycle, b) simulated specimen cooling fluxes diagram and c) the cooling fluxes curves.

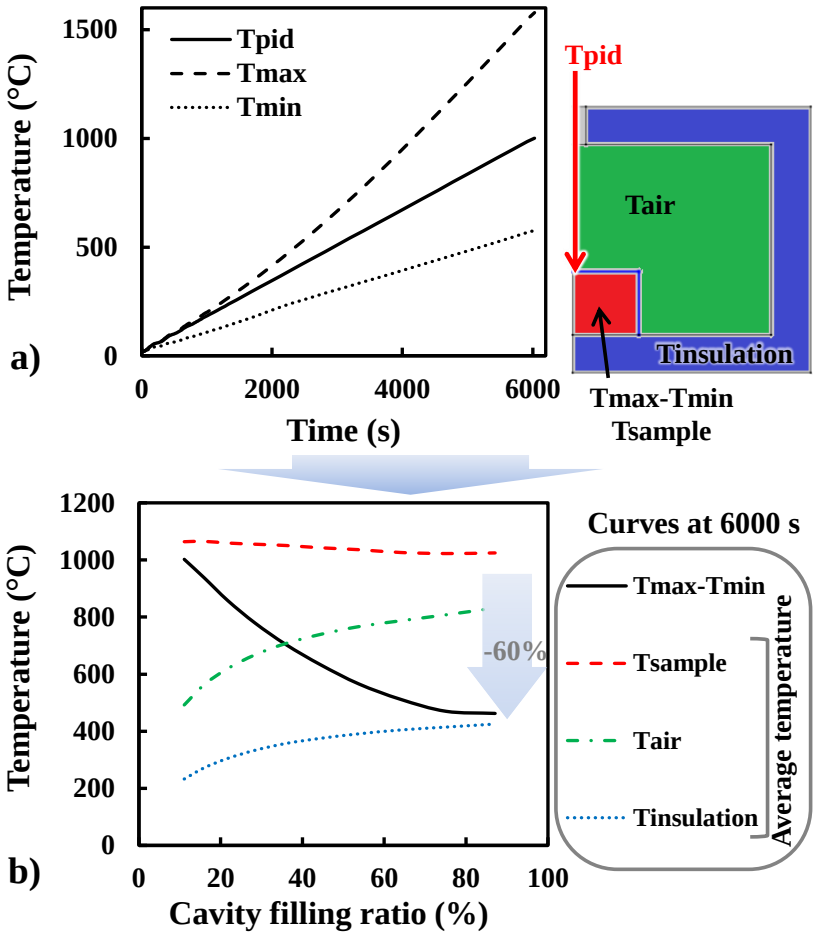

Figure 5 a) Simulated maximum, minimum and PID regulated specimen temperatures for the reference direct heating configuration (11% cavity filling ratio), b) simulated specimen maximum temperature difference and average specimen, air, insulation temperatures.

First of all, we can see from the simulated temperature field (figure 4a) and in (figure 5b) that the specimen temperature difference (Tmax-Tmin) varies from 1000 K to almost 400 K when the cavity filling is increased to more than 80%. In figure 4a, the convection velocity arrows almost disappear for high filling ratio. The 20% convective flux in figure 4b is essentially due to air conduction. Nevertheless, we should keep in mind that the diagrams in figure 4b just indicate the relative proportion of the specimen cooling fluxes. In order to explain the stabilization effect of the cavity filling ratio, we should compare directly the cooling fluxes curves reported in figure 4c. These fluxes curves indicate a clear decrease of the radiative and convective fluxes when increasing the cavity filling ratio. The convection fluxes are decreased because the air cavity space becomes very thin for high cavity filling ratio and the circular convection fluxes cannot be developed. On the other hand, the thin air distance between the

specimen and the insulation box leads to an increase of both the insulation box inner surface temperature and air temperature (figure 4a and figure 5b). These two temperatures tend to be very close to the sample temperature when increasing the cavity filling ratio. The radiative fluxes are then reduced for high cavity filling ratio as the insulation box inner surface irradiates a significant heat back to the specimen.

Increasing the cavity filling ratio contribute to a significant reduction of the convective/radiative cooling fluxes which improves the specimen homogeneity of 60% (in terms of temperature difference, Tmax-Tmin) compared to the reference direct heating configuration.

4.3. Heating rate stabilization effect

With higher heating rates, an improved temperature stabilization is expected by delaying the hot-spot formation. As hot spots originate from the cooling of the surfaces of the specimen, it is easy to figure out that the reduction of the heating time will end up with a lower total heat loss energy in the sample surfaces, and then, in the homogenization of the temperatures. We test here different heating rates from the reference direct heating case (10K/min figure 2) to 200 K/min. The results are reported in figure 6 and figure 7. The simulated temperature field in figure 6a and the curves in figure 7 shows that an increase of the heating rate decreases the air and insulation material temperature and homogenizes the specimen temperature where Tmax-Tmin goes from 1000 K for 10 K/min to 800 K for 200 K/min. This homogenization effect is weaker than the one previously discussed (cavity filling effect); however, the effect of the heating rate is not negligible.

The homogenization effect is not explained by the relative heat flux diagrams figure 6b but by the heat loss energy on the sample surfaces (see figure 6c). Compared to the previous case (cooling flux comparison), the present case on heating rates should take into account the

cooling time. We then choose to compare the cooling flux energy (in W.h) which represents the consumed energy through the specimen surfaces. These curves clearly indicate a high reduction of the total energy loss from the surface for high heating rates.

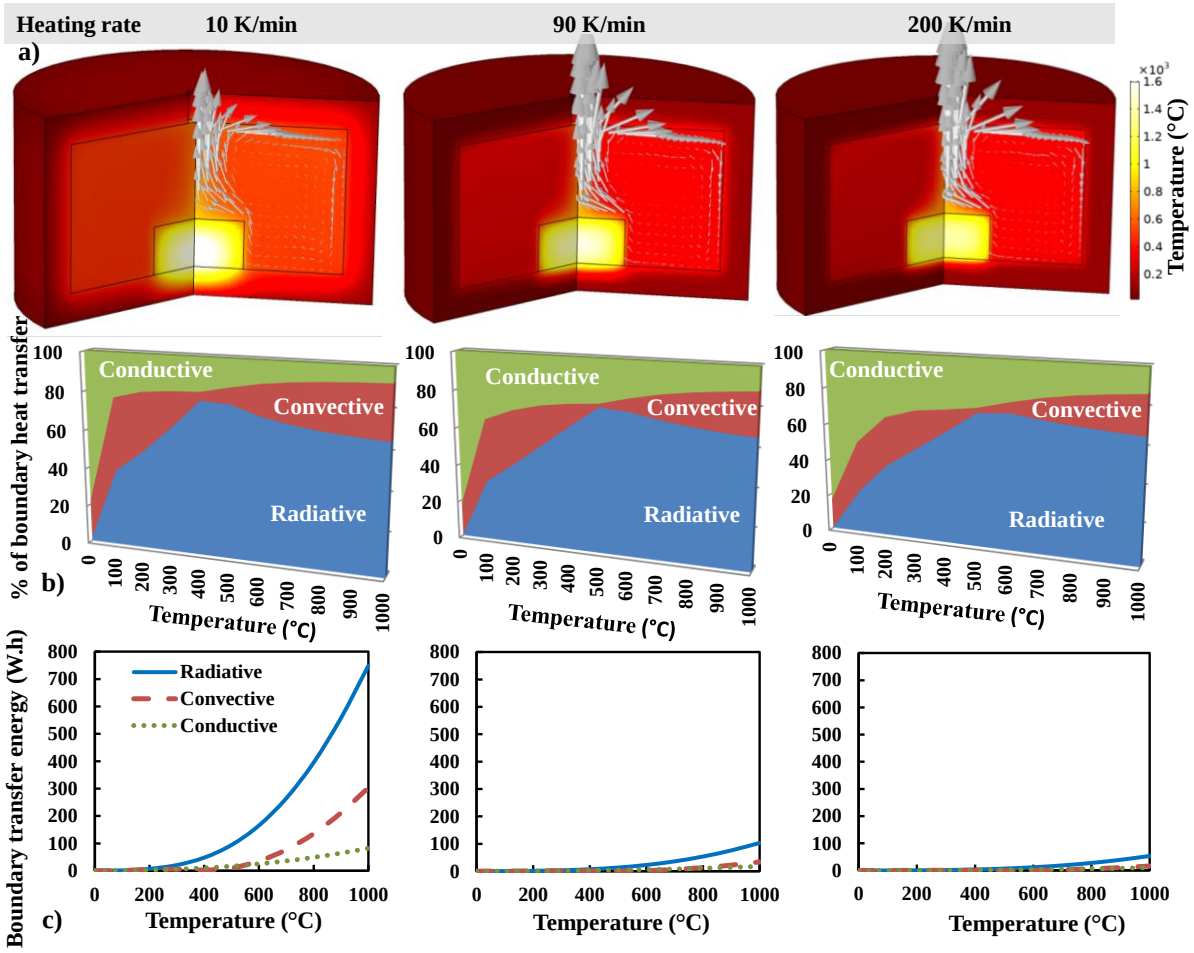

Figure 6 Simulation of the ETC configuration for different heating rate, a) simulated temperatures at the end of the cycle, b) simulated specimen cooling fluxes diagram and c) boundary heat transfer energy curves.

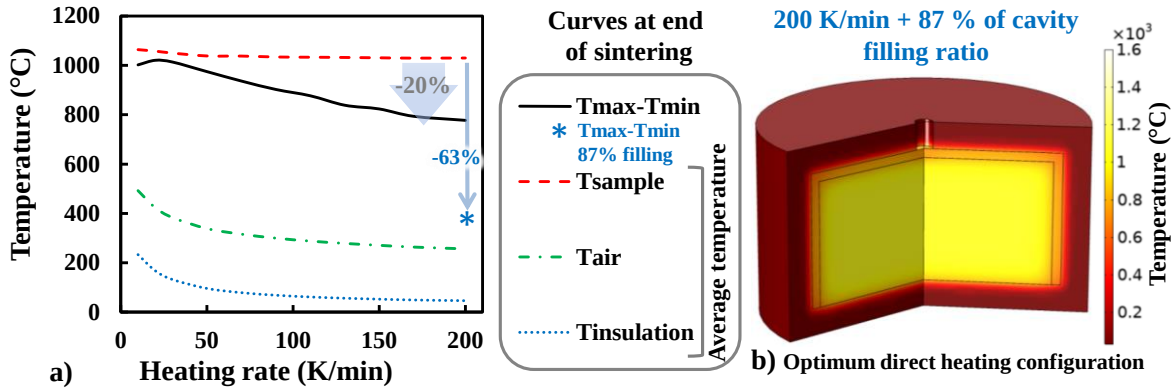

Figure 7 a) Simulated specimen maximum temperature difference and average specimen, air, insulation temperatures for different heating rates, b) simulated temperature field corresponding to high heating rate (200 K/min) and high cavity filling ratio (87 %).

The thermal heterogeneity remains high because we consider a low cavity filling configuration (11%). In this configuration, the cooling flux increases because the air and insulation temperatures remain at low temperatures for high heating rate (figure 6a and figure 7a). The weak homogenization for high heating rates, results from the delay of the hot spot formation (a time factor). As showed in figure 7b, it is possible to couple the high cavity filling case (87 %) with high heating rate (200 K/min). This coupling reduces the convective/radiative heat loss while delay the gradient formation which homogenize the system. The temperature difference in the sample is decreased of 63 % which is slightly better than the pure effect of high cavity filling ratio (figure 5b).

For direct heating, the cavity filling parameter can improve the sample homogeneity of 60%, high heating rate of 20% and both parameters of 63%. The results figure 7b can be compared to Biesuz et al [32] study on “thermally insulated flash sintering”, a configuration which combines high filling ratio (thermal insulation) and very high heating rates (>1000 K/min). They showed this configuration is more energy efficient and enhance densification while having a relatively homogeneous microstructure. Indeed, attaining stable high heating rate systems (like in the configuration figure 7b) is the main targeted challenge to favor interesting materials properties *via* methods like: two steps sintering[33], microwave sintering[22], flash sintering[18], *etc.* Nevertheless, temperature differences (in figure 7a) of a few 100 K are still

present due to the cooling through the insulation box and may disturb the sintering and generates distortions[15]. To efficiently homogenize the temperatures, a hybrid heating configuration is generally employed; this configuration is studied in the next section.

4.4. Hybrid heating

As shown in figure 1a, the susceptor is a ring of silicon carbide as it is usually employed in microwave sintering [24]. The heating of the zirconia specimen is imposed by a Q_{PID} heat source, which regulates the upper specimen temperature. Hybrid heating considers an additional heat source term $Q_{PID}.Fc$ in the susceptor. We will vary the multiplicative factor *Fc* from 1 to 10. The higher *Fc* is, the higher is the heat dissipation in the susceptor and lower is the relative dissipation in the zirconia specimen. For high *Fc*, the specimen is essentially heated by the susceptor, which tends to conventional heating. The results of simulated hybrid temperature field, heat fluxes and temperature curves are reported in figure 8, figure 9 and figure 10, respectively.

The simulation in figure 8 shows the circular convective flux motion is inverted compared to direct heating (figure 2) and corresponds to a convection motion that brings the energy from the susceptor ring to the zirconia specimen. The average temperature in figure 10 indicates that an increase of *Fc* raises the tooling and air temperatures. Therefore, the temperature distribution in the zirconia specimen is homogenized. At the end of the cycle, it must be noted for *Fc=1X* that a hot spot was developed (figure 8). This is due to the low external heat coming from the susceptor (not enough to homogenize the hot spot). The specimen temperature is regulated by the upper surface (see scheme in figure 5). However, if we compare the sample temperature distribution, in the beginning (600 s) and for high *Fc*, T_{PID} overestimates the specimen temperatures (external heating) while in the end (6000 s) and for low *Fc*, T_{PID} underestimates the specimen temperatures (hot spot). The temperature difference in the sample is significantly reduced for *Fc* higher than 4 (figure 10). Compared to the direct

case, the homogenization effect of hybrid heating is of 90% which is far higher than the impact of the cavity filling and heating rates in direct heating. The analysis of the specimen surfaces fluxes in figure 9a reveals, the low *Fc* is essentially governed by cooling fluxes (negative). In the transition (*Fc=4X*) and for high *Fc*, the radiative and convective fluxes stat to become positive meaning the specimen gains heat from the susceptor (external heating). The hybrid case at *Fc=4X* has a well-balanced heat flux between the heat produced in the specimen and the heat coming from the external part (susceptor). The transition of heating/cooling fluxes for *Fc=4X* generates the radiative/convective distribution obtained in figure 9b. In this case, at the beginning of the heating (600 s in figure 8), the heating is external but not excessively heterogeneous, which is interesting to allow an easy debinding of the polymeric phase usually present in green specimens. If the temperature is high in the center of the specimen, like in direct configuration (figure 2a), the debinding could make the specimen swells generating cracks. In hybrid configuration, at the end of the cycle (still for *Fc=4X* at 6000 s), the heating is homogeneous and the temperature differences do not exceed 100 K, which is required for an homogeneous sintering. The 'Tmax-Tmin' curve (figure 10) reveals that this temperature difference slightly increases for *Fc* value higher than 4X. This is due to the conductive cooling through the support which is not compensated by the specimen volume dissipation like in the *Fc=4X* case.

This study shows that a pure external heating can be less homogeneous than hybrid heating, even if conventional heating is anyway more homogeneous than pure direct heating. This characteristic is interesting as it justifies the interest of the Microwaves Assisted Technologies (MAT) which inject microwaves to assist the conventional sintering in furnaces[21,34]. This simulation reveals the ideal hybrid heating case is a situation where the susceptor heating behavior follows the specimen heating with a slight advance. To approach this ideal case experimentally, it is required to adjust the thermal dissipation in the susceptor by

composites/multimaterials approaches or by the addition of an external heating element. The ETC model developed here will be of great help to conduct this adjustment study.

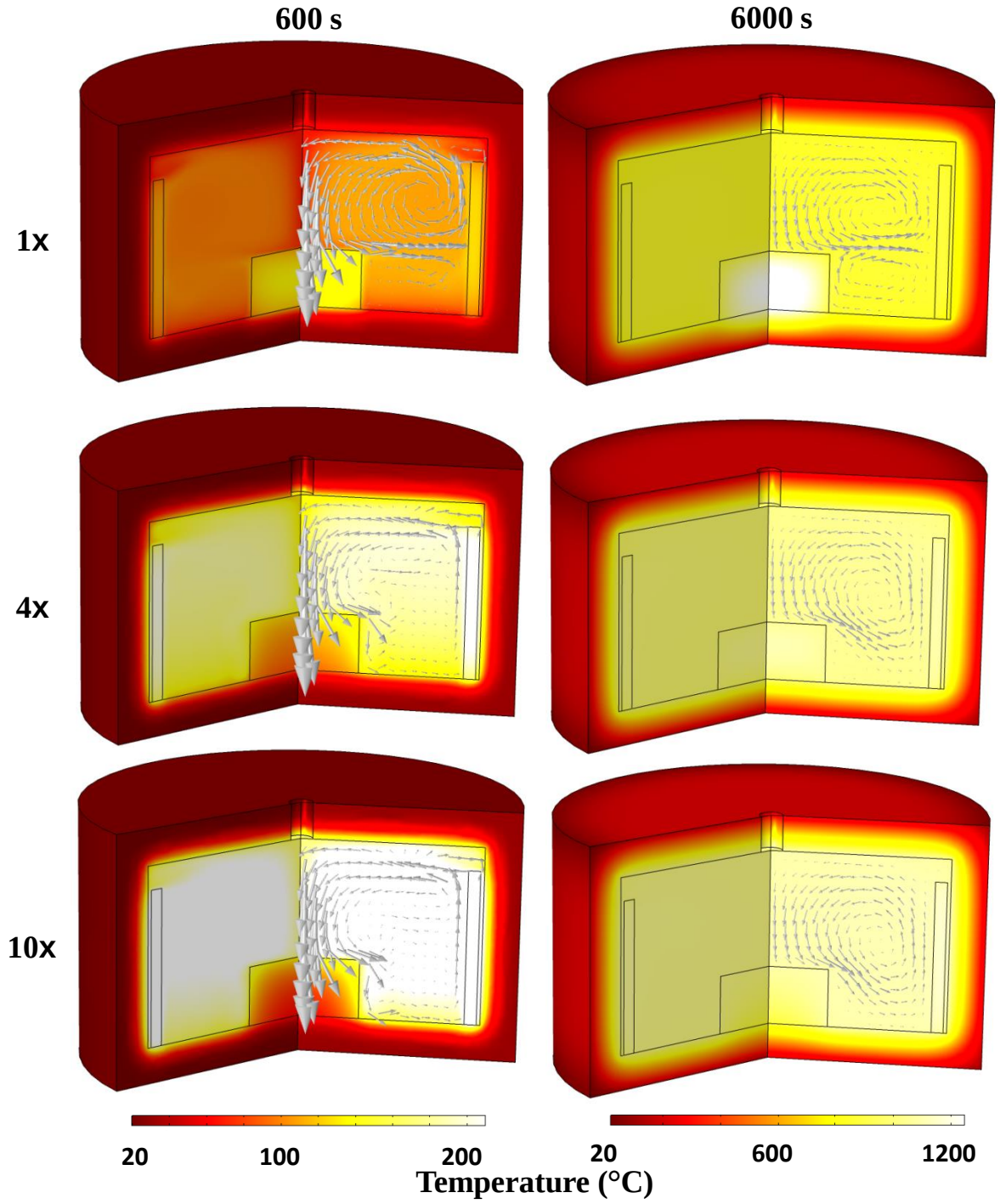

Figure 8 Simulated temperature field for hybrid heating ETC configurations using a volumetric heat dissipation in the susceptor ring multiplied by a factor of 1×, 4× and 10× the dissipation of the specimen.

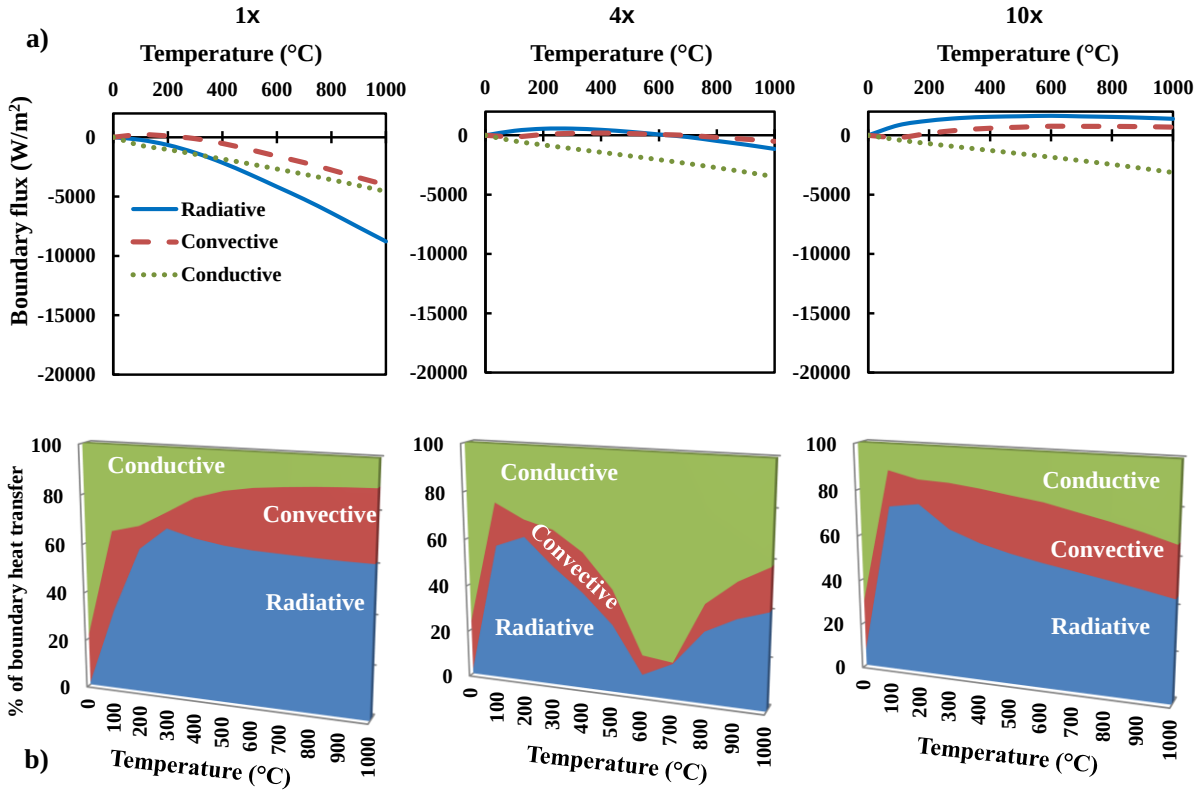

Figure 9 a) Boundary cooling fluxes curves and b) fluxes diagrams, for 1×, 4× and 10× hybrid heating configurations.

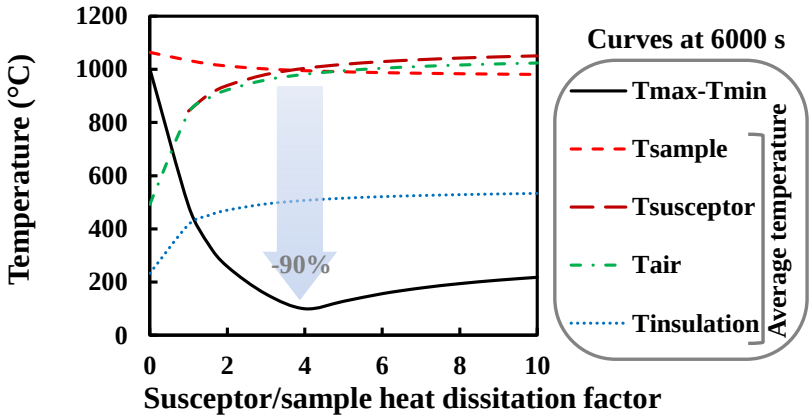

Figure 10 Simulated specimen maximum temperature difference and average specimen, air, insulation temperatures for different susceptor dissipation factor.

4.5. Microwave sintering experiment in direct hybrid configurations

In this section, we test experimentally the different hybrid and direct heating configurations. The aim is to observe the impact of the heating mode on the sintering of a zirconia sample, especially its homogeneity. Three microwaves sintering configurations were tested to study direct and hybrid heating stability. One is similar to the reference configuration (figure 2) where the zirconia specimen is directly heated in a large air volume (where convection cooling can easily develop). As suggested by section *4.2*, the heating can be significantly reduced for high cavity filling values (corresponding to a configuration close to thermal insulation). We test this "insulated direct" configuration by surrounding the sample with insulation material powder. Finally, we try the hybrid heating configuration using two silicon carbide plates. We choose a heating cycle of 40 K/min to 800 °C and 10 K/min for the sintering zone up to 1300 °C. The results are reported in figure 11. The "direct" sintering experiment which undergoes ~ 1000 K of temperature difference in the simulation (figure 2a) leads to the rapid destruction of the specimen (experimentally). As suggested in figure 4a, the "insulated direct" configuration is much more stable even if a small concave shape can be seen on the specimen surface indicating a higher temperature in the specimen center. As expected the "hybrid" configuration shows the most homogeneous results.

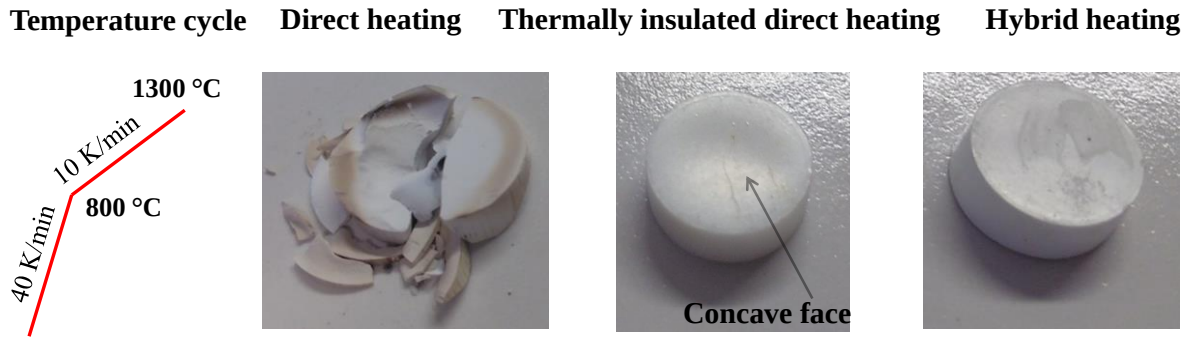

Figure 11 Direct, thermally insulated and hybrid microwave heating of 12 mm green zirconia specimen; the heating cycle imposed to all specimen surfaces is reported on the left.

5. Conclusion

Heating modes have a key impact on the homogeneity of the field assisted sintering (FAST) processes. We focus our approach on the simulation of direct and hybrid heating of a zirconia green specimen in an insulation box cavity, a classical case in microwave sintering. Our simulation work aims to study the impact of the surface to surface thermal radiation and the natural convection in the cavity on the homogeneity of the specimen heating. These parameters are classically approximated by analytical relations that highly idealize the complexity of the cavity heat exchanges. In the present simulations, the radiative fluxes take into account the radiative contribution coming from all surrounding surfaces in the inner cavity. The convective flux is also very important as it homogenizes the heating in all the cavity areas filled with air. We determine by our analysis that the specimen heating is influenced by conduction loss flux on the support which represents about 10% and convection/radiation exchanges flux in the inner cavity which represents about 30% and 60% respectively. In direct heating configuration, the thermal inhomogeneity generated by theses cooling fluxes induces the formation of a hot spot in the specimen center with temperature differences as high as 1000 K (from the center to the corner).

The parametric simulation analyses reveal that these heterogeneities can be reduced by three approaches. Lowering the air volume in the cavity is an efficient way to reduce the convective motion while raising the adjacent tooling temperatures which decreases 60% of the initial heterogeneity. High heating rates as an interesting potential to delay the hot spot formation and homogenize the temperatures, but this decreases only by 20% the initial heterogeneity. Hybrid heating is the most efficient way to homogenize up to 90% of the temperatures initial heterogeneity. The success of this approach lies in the heating balance between the heat generated in the sample volume and the external heat provided by the susceptor through radiative/convective fluxes. The microwave sintering experiments performed in similar

direct/hybrid configurations confirm the presence of an important hot spot in direct heating and homogeneous sintering in insulated direct and hybrid configurations.

The optimum heating configurations have been determined to be (i) a coupled conditions of high thermal insulation and high heating rate, for direct heating, and (ii) a hybrid configuration where the susceptor is adjusted to follow the specimen heating. The "Equivalent Thermal Cavity" (ETC) simulation developed in this study in an efficient way to study the heating stability of the highly varied FAST sintering approaches, where thermal gradient problems are often limiting the advanced material properties advantages.

Acknowledgements

The help and support of Christelle Bilot and Anthony Bilot is gratefully acknowledged.

References

[1] Bordia RK, Kang S-JL, Olevsky EA. Current understanding and future research directions at the onset of the next century of sintering science and technology. J Am Ceram Soc 2017;100:2314–52. https://doi.org/10.1111/jace.14919.

[2] Olevsky EA, Dudina D V. Field-Assisted Sintering. Cham: Springer International Publishing; 2018. https://doi.org/10.1007/978-3-319-76032-2.

[3] Orrù R, Licheri R, Locci AM, Cincotti A, Cao G. Consolidation/synthesis of materials by electric current activated/assisted sintering. Mater Sci Eng R Reports 2009;63:127–287. https://doi.org/10.1016/j.mser.2008.09.003.

[4] Bouvard D, Charmond S, Carry CP. Finite Element Modelling of Microwave Sintering, 2010, p. 171–80. https://doi.org/10.1002/9780470599730.ch17.

[5] Anselmi-Tamburini U, Gennari S, Garay JE, Munir ZA. Fundamental investigations on the spark plasma sintering/synthesis process. Mater Sci Eng A 2005;394:139–48. https://doi.org/10.1016/j.msea.2004.11.019.

[6] Vanmeensel K, Laptev A, Hennicke J, Vleugels J, Vanderbiest O. Modelling of the temperature distribution during field assisted sintering. Acta Mater 2005;53:4379–88. https://doi.org/10.1016/j.actamat.2005.05.042.

[7] Todd RI, Zapata-Solvas E, Bonilla RS, Sneddon T, Wilshaw PR. Electrical characteristics of flash sintering: thermal runaway of Joule heating. J Eur Ceram Soc 2015;35:1865–77. https://doi.org/10.1016/j.jeurceramsoc.2014.12.022.

[8] Dong Y, Chen I-W. Thermal Runaway in Mold-Assisted Flash Sintering. J Am Ceram Soc 2016;99:2889–94. https://doi.org/10.1111/jace.14413.

[9] Giuntini D, Olevsky E, Garcia-Cardona C, Maximenko A, Yurlova M, Haines C, et al. Localized Overheating Phenomena and Optimization of Spark-Plasma Sintering Tooling Design. Materials (Basel) 2013;6:2612–32. https://doi.org/10.3390/ma6072612.

[10] Demirskyi D, Vasylkiv O. Hot-spots generation, exaggerated grain growth and mechanical performance of silicon carbide bulks consolidated by flash spark plasma sintering. J Alloys Compd 2017;691:466–73. https://doi.org/10.1016/j.jallcom.2016.08.234.

[11] Marinel S, Savary E, Gomina M. Sintering of CuO and ZnO in a Single Mode Microwave Cavity with Shrinkage Control. J Microw Power Electromagn Energy 2010;44:57–63. https://doi.org/10.1080/08327823.2010.11689770.

[12] Dong Y. On the Hotspot Problem in Flash Sintering. ArXiv 2017:1702.05565.

[13] Manière C, Zahrah T, Olevsky EA. Inherent heating instability of direct microwave sintering process: Sample analysis for porous 3Y-ZrO2. Scr Mater 2017;128:49–52. https://doi.org/10.1016/j.scriptamat.2016.10.008.

[14] Yakovlev V V, Allan SM, Fall ML, Shulman HS. Computational Study of Microwave Processing of thermal runaway in microwave processing Zirconia. In: Tao JCE, editor. Microw. RF Power Appl., Toulouse: 2011, p. 303–6.

[15] Manière C, Zahrah T, Olevsky EA. Fully coupled electromagnetic-thermal-mechanical comparative simulation of direct vs hybrid microwave sintering of 3Y-ZrO2. J Am Ceram Soc 2017;100:2439–2450. https://doi.org/10.1111/jace.14762.

[16] Cologna M, Rashkova B, Raj R. Flash Sintering of Nanograin Zirconia in <5 s at 850°C. J Am Ceram Soc 2010;93:3556–9. https://doi.org/10.1111/j.1551-2916.2010.04089.x.

[17] Yu M, Grasso S, Mckinnon R, Saunders T, Reece MJ. Review of flash sintering: materials, mechanisms and modelling. Adv Appl Ceram 2017;116:24–60.

https://doi.org/10.1080/17436753.2016.1251051.

[18] Biesuz M, Sglavo VM. Flash sintering of ceramics. J Eur Ceram Soc 2019;39:115–43. https://doi.org/10.1016/j.jeurceramsoc.2018.08.048.

[19] Zhang Y, Jung J-I, Luo J. Thermal runaway, flash sintering and asymmetrical microstructural development of ZnO and ZnO–Bi2O3 under direct currents. Acta Mater 2015;94:87–100. https://doi.org/10.1016/j.actamat.2015.04.018.

[20] Manière C, Lee G, Olevsky EA. All-Materials-Inclusive Flash Spark Plasma Sintering. Sci Rep 2017;7:15071. https://doi.org/10.1038/s41598-017-15365-x.

[21] Oghbaei M, Mirzaee O. Microwave versus conventional sintering: A review of fundamentals, advantages and applications. J Alloys Compd 2010;494:175–89. https://doi.org/10.1016/j.jallcom.2010.01.068.

[22] Rybakov KI, Olevsky EA, Krikun E V. Microwave Sintering: Fundamentals and Modeling. J Am Ceram Soc 2013;96:1003–20. https://doi.org/10.1111/jace.12278.

[23] Thuault A, Savary E, Bazin J, Marinel S. Microwave sintering of large size pieces with complex shape. J Mater Process Technol 2014;214:470–6. https://doi.org/10.1016/j.jmatprotec.2013.09.030.

[24] Heuguet R, Marinel S, Thuault A, Badev A. Effects of the Susceptor Dielectric Properties on the Microwave Sintering of Alumina. J Am Ceram Soc 2013;96:3728–36. https://doi.org/10.1111/jace.12623.

[25] Santos T, Valente MA, Monteiro J, Sousa J, Costa LC. Electromagnetic and thermal history during microwave heating. Appl Therm Eng 2011;31:3255–61. https://doi.org/10.1016/j.applthermaleng.2011.06.006.

[26] Santos T, Costa LC, Hennetier L, Valente MA, Monteiro J, Sousa J. Microwave processing of porcelain tableware using a multiple generator configuration. Appl Therm Eng 2013;50:677–82. https://doi.org/10.1016/j.applthermaleng.2012.07.010.

[27] Manière C, Chan S, Olevsky EA. Microwave sintering of complex shapes: From multiphysics simulation to improvements of process scalability. J Am Ceram Soc 2019;102:611–20. https://doi.org/10.1111/jace.15892.

[28] Manière C, Zahrah T, Olevsky EA. Fluid dynamics thermo-mechanical simulation of sintering: Uniformity of temperature and density distributions. Appl Therm Eng 2017;123:603–13. https://doi.org/10.1016/j.applthermaleng.2017.05.116.

[29] Egorov S V., Rybakov KI, Semenov VE, Bykov Y V., Kanygina ON, Kulumbaev EB, et al. Role of convective heat removal and electromagnetic field structure in the microwave heating of materials. J Mater Sci 2007;42:2097–104.

https://doi.org/10.1007/s10853-006-0157-x.

[30] Bernardi C, Métivet B, Pernaud-Thomas B. Couplage des équations de Navier-Stokes et de la chaleur : le modèle et son approximation par éléments finis. ESAIM Math Model Numer Anal 1995;29:871–921.

[31] Tosoh zirconia powder 2020. https://www.rbhltd.com/wp-content/uploads/2019/05/Tosoh-Zirconia-Brochure.pdf.

[32] Biesuz M, Dong J, Fu S, Liu Y, Zhang H, Zhu D, et al. Thermally-insulated flash sintering. Scr Mater 2019;162:99–102. https://doi.org/10.1016/j.scriptamat.2018.10.042.

[33] Chen I-W, Wang X-H. Sintering dense nanocrystalline ceramics without final-stage grain growth. Nature 2000;404:168–71. https://doi.org/10.1038/35004548.

[34] Wroe R, Rowley AT. Evidence for a non-thermal microwave effect in the sintering of partially stabilized zirconia. J Mater Sci 1996;31:2019–26. https://doi.org/10.1007/BF00356621.

Figure captions

Figure 1 a) Scheme of the equivalent thermal cavity with the values of the boundary parameters, b) mesh.

Figure 2 Direct 10 K/min heating of a zirconia specimen; a) temperature and b) convection velocity field at the end of the cycle; c) scheme of the specimen interfaces considered in the specimen cooling fluxes analysis, d) integral of the specimen cooling fluxes through the specimen surfaces, e) cooling fluxes ratio diagram.

Figure 3 Direct 10 k/min heating configuration in vacuum (without convection), a) simulated temperature field at the end of the cycle and b) the simulated specimen cooling fluxes diagram.

Figure 4 Simulation of the ETC configuration for different cavity filling ratio, a) simulated temperatures at the end of the cycle, b) simulated specimen cooling fluxes diagram and c) the cooling fluxes curves.

Figure 5 a) Simulated maximum, minimum and PID regulated specimen temperatures for the reference direct heating configuration (11% cavity filling ratio), b) simulated specimen maximum temperature difference and average specimen, air, insulation temperatures.

Figure 6 Simulation of the ETC configuration for different heating rate, a) simulated temperatures at the end of the cycle, b) simulated specimen cooling fluxes diagram and c) boundary heat transfer energy curves.

Figure 7 a) Simulated specimen maximum temperature difference and average specimen, air, insulation temperatures for different heating rates, b) simulated temperature field corresponding to high heating rate (200 K/min) and high cavity filling ratio (87 %).

Figure 8 Simulated temperature field for hybrid heating ETC configurations using a volumetric heat dissipation in the susceptor ring multiplied by a factor of 1×, 4× and 10× the dissipation of the specimen.

Figure 9 a) Boundary cooling fluxes curves and b) fluxes diagrams, for 1×, 4× and 10× hybrid heating configurations.

Figure 10 Simulated specimen maximum temperature difference and average specimen, air, insulation temperatures for different susceptor dissipation factor.

Figure 11 Direct, thermally insulated and hybrid microwave heating of 12 mm green zirconia specimen; the heating cycle imposed to all specimen surfaces is reported on the left.